Modeling the effect of free convection on permafrost melting-rates in frozen rock-clefts

Amir Sedaghatkish[1,2], Frédéric Doumenc[3,4], Pierre-Yves Jeannin[1], Marc Luetscher[1]

[1]Swiss Institute for Speleology and Karst Studies (SISKA), CH-2300, La Chaux-de-Fonds, Switzerland
[2]Center for Hydrogeology and Geothermics (CHYN), University of Neuchâtel, 2000 Neuchâtel, Switzerland
[3]Univèrsité Paris-Saclay, CNRS, FAST, 91405, Orsay, Rue André Rivière, France
[4]Sorbonne Université, UFR 919, 4 place Jussieu, F-75252, Paris Cedex 05, France

Correspondence to: Amir Sedaghatkish (amir.sedaghatkish@isska.ch)

Abstract. This research develops a conceptual model of a karst system subject to mountain permafrost. The transient thermal response of a frozen rock-cleft after the rise of the atmosphere temperature above the melting temperature of water is investigated by numerical simulations. Free convection in liquid water (i.e., buoyancy-driven flow) is considered. The density increase of water from 0 to 4℃ causes warmer meltwater to flow downwards and colder upwards, resulting in significant enhancement of the heat transferred from the ground surface to the melting front. Free convection increases the melting rate by approximately an order of magnitude compared to a model based on thermal conduction in stagnant water. The model outcomes are compared qualitatively with field data from Monlesi ice cave (Switzerland) and confirm the agreement between real-world observations and the proposed model when free convection is considered.

Keywords: Numerical modeling, free convection, melting rate, conduction, permafrost, karst, cave, hydrogeology

1 Introduction

With global climate change and rising temperatures, permafrost degradation has become a significant concern (Duvillard et al., 2021; Walvoord and Kurylyk, 2016; Jin et al., 2021). This is particularly true in mountain regions where rapid thawing causes subsidence and rockfalls impacting construction works and tourist facilities (Haeberli et al., 2017). Thawing permafrost poses serious challenges to infrastructures built on frozen ground, including buildings, roads, pipelines, and railways. (Larsen et al., 2008; Cheng, 2005; Pham et al., 2008; Zhang et al., 2005; Fortier et al., 2011). Permafrost acts as a natural barrier, preventing water from infiltrating into the ground. As it thaws, drainage patterns are altered, leading to increased erosion and discharge of groundwater to rivers and lakes (Bense et al., 2012; Andresen et al., 2020; Fabre et al., 2017; Painter et al., 2016;

30 Walvoord and Kurylyk, 2016). Permafrost degradation can also disrupt ecosystems adapted to frozen conditions. Trees, plants, and wildlife that rely on permafrost stability may struggle to adapt to climate changes, leading to shifts in species distribution and ecosystem dynamics depending on the permafrost melting rate (Hayward et al., 2018; Krumhansl et al., 2015; Pelletier et al., 2018).

Field measurements in boreholes (e.g. Noetzli et al., 2021; Haberkorn et al., 2021) and caves (Luetscher et al., 2008; Colucci
35 and Guglielmin, 2019; Wind et al., 2022) have shown that heat advected by water and air fluxes may significantly disturb the geothermal field, challenging classical models of heat propagation based on conductive fluxes. In carbonate environments, in particular, the infiltration of water along well-developed conduits may develop a thermal anomaly deep into the karst system. The discontinuous nature of permafrost in karst environments may lead to the formation of massive cave ice at depth (Bartolomé et al., 2022) but also explain unexpected speleothem formations during glacial times (Luetscher et al., 2015;
40 Fohlmeister et al., 2023; Fohlmeister et al., 2023)

Efforts are being made to study and understand permafrost degradation to mitigate its impacts. So far, most studies considered mainly conductive and latent heat fluxes (Malakhova, 2022; Galushkin, 1997; Ivanov and Rozhin, 2022; Marchenko et al., 2008; Schuster et al., 2018; Jafarov et al., 2012; Cicoira et al., 2019; Hornum et al., 2020). Such models are, however, not applicable to heterogeneous, ice-rich media including debris-slopes, rock glaciers, fractured and/or karst aquifers. But, even
45 though conventional 1D transient models are not suitable to every context, they offer several advantages including lower computational costs than 2 or 3D models and easy implementation. Pruessner et al., (2021) investigated glacier runoff associated with permafrost degradation in high Alpine catchments. They used two different methods GERM (Huss et al., 2008) and SNOWPACK (Bartelt and Lehning, 2002) which are based on 1D transient conduction considering latent heat exchanges, different thermal properties of ground layers constituents and ventilation effects. This distributed model is efficient for
50 calculation of temperature in large domains (catchment scale). Mohammed et al., (2021) developed a hydro-thermal-solutal model for analyzing reactive solute transport in permafrost-affected groundwater system by considering convective flux in the energy balance. Tubini et al., (2021) proposed a numerical approach for modeling heat transfer of permafrost thawing based on conduction and latent heat flux in 1D domain which is capable to deal with high time steps and maintains conservation of energy in long-term simulations. Hasler et al., (2011) built a conceptual model combining numerical modeling and laboratory
55 experiments to investigate the effect of advective heat transport induced by water drainage in frozen rock clefts and fractures at small scales. They built a conceptual model combining numerical modelling and laboratory experiments. These authors find a significant effect of water flow inside the clefts, due to the formation of thermal shortcuts between the atmosphere and the subsurface.

Although, the majority of these studies are designed to address large-scale problems they typically neglect free convection
60 within the liquid water phase. This process could nonetheless play an important role in the total heat transfer particularly in geographically restricted areas subject to mountain permafrost (Haberkorn et al., 2021). Figure 1-a displays the bottom of a frozen cleft hosted in an Alpine karst. Such clefts and fissures are characterized by distinct geometries accommodating contrasted volumes of ice. Our aim is to study the effect of free convection on the melting rate in frozen rock clefts and/or

karst conduits at daily scale. Atmospheric warming at the upper boundary melts the ice from top of the fractures, and increases the meltwater temperature. While most fluids expand as temperature increases, liquid water shrinks when warmed from 0°C to 4°C. Above this temperature, the common behavior is recovered (see the maximum density at 4°C in Fig.2). Therefore, the progressive warming of the meltwater at the top of the cleft results in an unstable situation (heavier fluid above lighter) that triggers free convection (buoyancy-driven flow). To assess the thermal reaction time, and thus hydrological breakthrough associated with the thawing of mountain permafrost we model the heat exchange in a frozen rock cleft. We assess by numerical simulations the temperature field in the meltwater, ice, and surrounding rock, as well as the velocity field within the liquid water to elucidate the main mechanisms driving the thawing of ice. Although a physical monitoring of such processes is hardly possible, our model fits as close as possible to effective field observations. A systematic comparison is conducted under similar thermal settings for two cases: one considers heat conduction in stagnant liquid water (SLW) whereas free convection (FC) is taken into account in the second case. Our study shows how free convection enhances the melting rate of an ice cleft at different aperture sizes.

2 Computational domain and governing equations

2.1 Physical model and simplifying assumptions

We consider the upper part of a single vertical cleft of size aperture A_p filled with pure water whose melting point is $T_m = 0°C$. This cleft is surrounded by a rock mass of width W (see Fig.1-b). In karst massifs, water flow concentrates in well-defined conduits (Ford and Williams, 2007). The micro-porosity of the rock is thus disregarded, and impermeable rock mass is assumed.

The cleft is located at the center of the 2D domain of height H_{dom}. In the initial state, the system (water and surrounding rock) is at the uniform initial temperature T_i=-1°C, and all the water is frozen. At time t=0, the temperature of the ground surface T_s increases at the constant rate 1.77 °C/hour to reach 15°C after 9 hours. This temperature increase is similar to the daily warming between the early morning and the afternoon.

The effect of the cleft aperture size was investigated by varying A_p from 2 cm to 50 cm. We imposed H_{dom}=0.8 m and W=1 m in all simulations. These values are large enough so that the thermal perturbation induced by the presence of the cleft does not reach the domain boundaries at the end of the simulated time (9 hours). The vertical and bottom boundaries of the domain can therefore be considered as adiabatic (see Fig.1-b). It is important to note that the domain height H_{dom} contains only the upper part of the cleft, whose actual depth commonly ranges from 1 to 10 m. The value of H_{dom} used in this study is convenient for the daily time scale considered in the numerical simulations. Simulating larger time scales would require larger values of H_{dom}.

2.2 Governing equations

The temperature T is the only dependent variable in the impermeable rock domain. It satisfies the standard heat equation

$$\rho_r c_{p,r} \frac{\partial T}{\partial t} = k_r \left(\frac{\partial^2 T}{\partial x^2} + \frac{\partial^2 T}{\partial z^2} \right) \tag{1}$$

95

where ρ_r, $c_{p,r}$ and k_r are the rock density, specific heat and thermal conductivity, respectively. z is the depth and x the horizontal distance from the symmetry plane of the cleft (see Fig. 1-b).

The water domain is more intricate. The velocity field must be calculated in the liquid part of the domain, but reduces to zero in the frozen region. To avoid the difficult task consisting in tracking the moving boundary between ice and liquid water, we

100 adopted a strategy that allows to define the same set of dependent variables and governing equations in the entire water domain. To this end, we do the approximation of smooth phase transition between solid and liquid phases. We assume that ice melting begins à temperature $T_{m1} = T_m - \Delta T$ and ends at $T_{m2} = T_m + \Delta T$ (water is in solid state for $T < T_{m1}$, in liquid state for $T < T_{m2}$, and both phases coexist for $T_{m1} \leq T \leq T_{m2}$). It is important to note that in this study, ΔT is a numerical parameter with no physical meaning. Ideally, the behavior of a pure substance melting at temperature T_m would be recovered for $\Delta T \rightarrow$

105 0. Decreasing ΔT thus improves model accuracy, but requires more computational resources (see Nazzi Ehms et al (2019) and Caggiano et al (2018) for more details).

The dependent variables defined in the water domain are the temperature T, the horizontal and vertical components of the velocity vector u and v, the pressure p and the liquid volume fraction θ. Because of the assumption of smooth phase transition, θ varies continuously from 0 (solid phase) to 1 (liquid phase) throughout the water domain (see Fig.1-b). The corresponding

110 governing equations read:

$$\frac{\partial u}{\partial x} + \frac{\partial v}{\partial z} = 0 \tag{2}$$

$$\rho_0 \frac{\partial u}{\partial t} + \rho_0 \left(u \frac{\partial u}{\partial x} + v \frac{\partial u}{\partial z} \right) = -\frac{\partial p}{\partial x} + \mu \left(\frac{\partial^2 u}{\partial x^2} + \frac{\partial^2 u}{\partial z^2} \right) + A \frac{(1-\theta)^2}{\theta^3 + \varepsilon} u \tag{3}$$

$$\rho_0 \frac{\partial v}{\partial t} + \rho_0 \left(u \frac{\partial v}{\partial x} + v \frac{\partial v}{\partial z} \right) = -\frac{\partial p}{\partial z} + \mu \left(\frac{\partial^2 v}{\partial x^2} + \frac{\partial^2 v}{\partial z^2} \right) - \rho_0 g \beta (T - T_0) + \rho_0 g + A \frac{(1-\theta)^2}{\theta^3 + \varepsilon} v \tag{4}$$

$$\rho c_p \frac{\partial T}{\partial t} + \rho c_p \left(u \frac{\partial T}{\partial x} + v \frac{\partial T}{\partial z} \right) - k \left(\frac{\partial^2 T}{\partial x^2} + \frac{\partial^2 T}{\partial z^2} \right) = 0 \tag{5}$$

$$\theta = \begin{cases} 0 & T < T_{m1} \quad \text{(Solid)} \\ \dfrac{T - T_{m1}}{T_{m2} - T_{m1}} & T_{m1} \leq T \leq T_{m2} \quad \text{(Diphasic)} \\ 1 & T > T_{m2} \quad \text{(Liquid)} \end{cases} \tag{6}$$

This set of equations includes the mass balance Eq.(2), the momentum balance Eqs.(3-4), the energy balance Eq.(5) and the relation between the liquid volume fraction θ and the temperature field Eq.(6). g is the gravity acceleration, ρ_0 is the density of liquid water at the reference temperature T_0, μ and β are the dynamic viscosity and thermal expansion coefficient of liquid water, ρ, c_p and k are the density, specific heat and thermal conductivity of water.

The last term in Eqs.(3-4) is used to impose the velocity transition between the liquid and solid phases. A and ε are numerical parameters imposed by the user. A must be as large as possible provided that solver stability is insured. In contrast, ε is a small parameter used to prevent divisions by zero in numerical calculations (Mousavi Ajarostaghi et al., 2019). It can be demonstrated that for $\theta = 0$ (i.e., in the solid phase), the solution of Eqs.(2-4) turns to $u \simeq v \simeq 0$, which is the solution expected in the solid phase (see Nazzi Ehms et al (2019) and Caggiano et al (2018) for more details). Conversely, the last term in Eqs.(3-4) vanishes for $\theta = 0$ (i.e., in the liquid phase). In this case, Eqs.(3-4) turns to the standard Navier-Stokes equations (momentum balance in an incompressible Newtonian fluid), required to calculate the velocity field in the liquid phase.

The boundary conditions are as follows. At the interface between an impermeable solid and a viscous fluid, the fluid velocity is equal to that of the solid (Guyon et al., 2015). This is the so-called no-slip and impermeability conditions, resulting in $u = v = 0$ at the rock-water interface. The temperature continuity and the heat flux conservation through this interface are also considered (since the water velocity vanishes at the rock-water interface, the heat flux through the interface reduces to conduction). As already mentioned in section 2.1, the bottom and vertical external boundaries are adiabatic, and the temperature evolution of the top boundary T_s increases at a constant rate (see Fig.1-b).

2.3 Material properties

The physical properties used in the simulations are listed in Table_1. Subscripts "r", "s" and "l" refer to rock, ice and liquid water respectively. No subscript indicates the effective properties considered in the water domain (solid, liquid, or diphasic). They are estimated from the liquid volume fraction θ as follows:

$$\rho = \rho_s (1-\theta) + \rho_l \theta \tag{7}$$

$$k = k_s (1-\theta) + k_l \theta \tag{8}$$

$$c_p = \frac{\rho_s c_{p,s} (1-\theta) + \rho_l c_{p,l} \theta}{\rho} + L_m \frac{\partial \alpha_m}{\partial T} \quad \text{with} \quad \alpha_m = \frac{1}{2} \frac{\rho_l \theta - \rho_s (1-\theta)}{\rho_l \theta + \rho_s (1-\theta)} \tag{9}$$

$$\mu = \mu_l \tag{10}$$

The effective specific heat c_p defined in Eq.(9) takes into account the latent heat of melting L_m. In the momentum equations Eqs.(3-4), the expansion coefficient β in the buoyancy term responsible for free convection is estimated from the relation

$$\beta = -\frac{1}{\rho_l}\frac{d\rho_l}{dT} \tag{11}$$

where ρ_l is the liquid water density displayed in Fig.2 (the order of magnitude of β in the unstable temperature range from 0 to 4°C is approximately -3×10^{-5} K^{-1}). Following the standard Boussinesq approximation (Bejan, 2013), constant density ρ_0 estimated at the reference temperature T_0 is considered in the inertia terms of Eqs.(3-4) ($\rho_0 = 999.84$ kg/m^3 at $T_0 = 0$°C). The Boussinesq approximation is valid if the maximum fluid density variation $\Delta\rho_l$ is much lower than the liquid density ρ_l, a condition usually satisfied in liquids ($\Delta\rho_l/\rho_l \sim 10^{-3}$ in our case).

The density of water is greater than that of ice by approximately 10%. This induces a reduction of volume upon melting, which is neglected in our model. This is equivalent to assume that an external water flow replenishes the top layer domain with water at the ground surface temperature T_s. This would result in the additional vertical velocity in the liquid phase (Heitz and Westwater, 1970):

$$v_l = \frac{(\rho_l - \rho_s)}{\rho_l}\frac{dH}{dt} \tag{12}$$

This velocity would be that of the liquid in the absence of free convection, or would be added to the free convection velocity field in the other case. This contraction-induced flow can be neglected if the heat advected in that way is negligible compared to the heat absorbed by the motion of the melting front:

$$\rho_l\, v_l\, c_{pl}(T_s - T_m) \ll L_m\rho_s\frac{dH}{dt} \tag{13}$$

Eqs.(12-13) yield the condition of validity:

$$\frac{(\rho_l - \rho_s)}{\rho_s}\frac{c_{pl}(T_s - T_m)}{L_m} \ll 1 \tag{14}$$

With the physical properties of table 1 and $T_s - T_m = 15$°C, the LHS of Eq.(14) is approximately equal to 0.02, much lower than 1. The contraction-induced flow can thus be safely neglected (see Heitz and Westwater (1970) for a comparison of mathematical solutions with equal and unequal phase densities).

2.4 Numerical methods

155 The system of partial differential equations (Eqs. 1-6) was solved by finite elements using the software Comsol Multiphysics version 6.0 (Galerkin method with quadratic Lagrangian elements, time discretization by implicit backward differentiation formula).

The mesh density close to the walls was refined due to the high gradient of velocity and a structured (mapped) mesh type was used for the water-ice domain as shown in Fig. 1-c. The mesh was validated by a sensitivity analysis comparing four different

160 mesh qualities, with 14,000, 24,000, 32,000, and 47,000 elements, respectively. The difference in the results between the latter three cases was found to be insignificant. The mesh with 24,000 elements was thus selected in all simulations.

Regarding the numerical parameters required to model melting, we imposed ΔT=0.5 °C, A =1000 kg.m^{-3}.s^{-1} and $\varepsilon = 10^{-3}$. We checked that imposing $\Delta T = 0.3$ °C or 0.7 °C did not significantly change the results (see Appendix A). The selected

165 values of A and ε produced vanishingly small velocity fields in the ice with no deterioration of the solver stability.
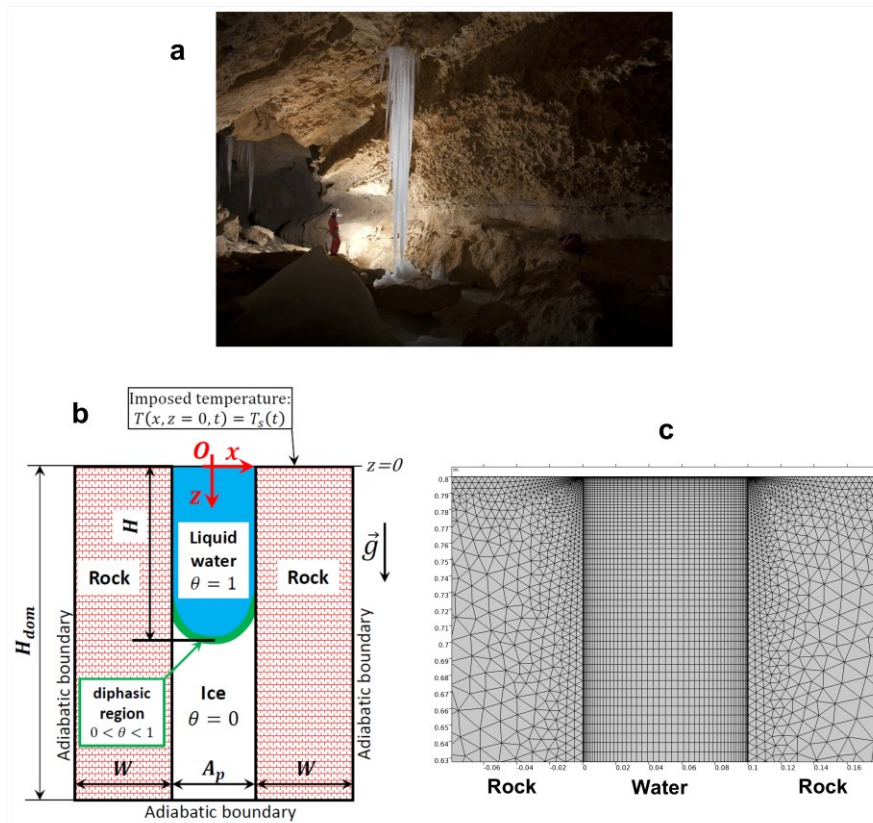
Figure 1. a) Pingouins cave, Switzerland, showing ice-filled clefts exposed on the cave roof (Photo courtesy A. Conne) b) Computational domain with external boundary conditions; 2 cm $\leq A_p \leq$ 50 cm, H_{dom}=0.8 m and W_{dom}=1 m (the sketch is not at scale) c) Finite element mesh in the upper part of the computational domain.

Table 1. Thermal properties and numerical parameters. The liquid water properties are temperature dependent. The properties of ice and rock are assumed constant.

Thermal properties	values	Reference
ρ_s (kg/m³)	916.2	-
k_s (W/m/K)	2.22	-
$c_{p,s}$ (J/kg/K)	2050	-
ρ_l (kg/m³)	see Fig.2	(Comsol, 2018)
k_l (W/m/K)	0.556 at 0°C 0.585 at 15°C	(Comsol, 2018)
$c_{p,l}$ (J/kg/K)	4216 at 0°C 4192 at 15°C	(Comsol, 2018)
μ_l (mPa.s)	1.79 at 0°C 1.43 at 7.5°C 1.15 at 15°C	(Comsol, 2018)
ρ_r (kg/m³)	2320	(Covington et al., 2011)
k_r (W/m/K)	1.656	(Guerrier et al., 2019)
$c_{p,r}$ (J/kg/K)	810	(Covington et al., 2011)
L_m (J/kg)	334000	(Weast, 1986)

170
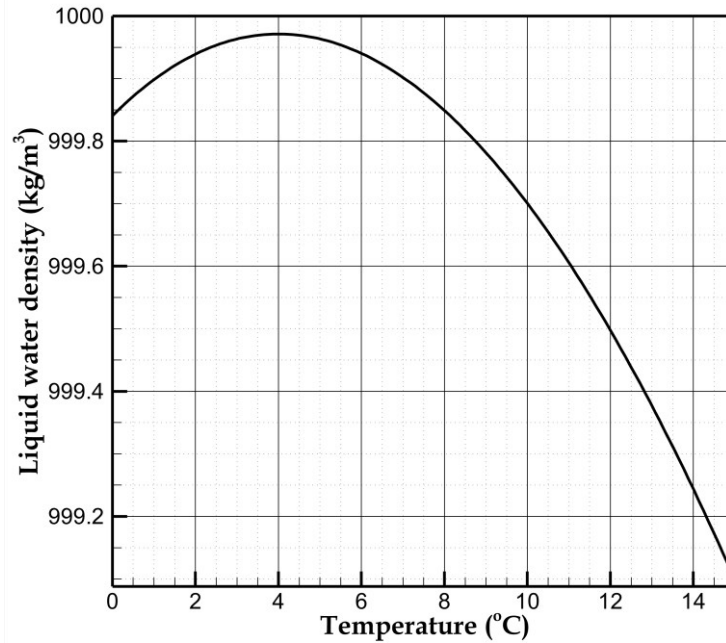
Figure 2. density of liquid water as a function of temperature.

3 Model validation

175 The validity of our model is tested by comparison with two studies from the literature. A simple test case assuming stagnant liquid water (no free convection) was selected as a first step (numerical simulation of ice freezing by Kahraman et al., 1998). In a second step, our model was tested against experimental results including free convection (ice melting experiment by Virag et al., 2006).

3.1 Stagnant liquid water

180 When free convection is neglected, conduction and latent heat fluxes are the only mechanisms transferring heat in liquid water and ice. We compare our results with the results from (Kahraman et al., 1998). These authors developed a model to examine the heat transfer of ice melting inside a 20 cm×20 cm square assuming stagnant liquid water. A brief description of their conceptual model is given in Fig. 3-a. Ice is at an initial temperature of -30°C and is exposed to a temperature of 20 °C over half of the lower boundary ($0 \leq x \leq 10$ cm , $y = 0$ cm) and 70°C over the other half ($10 \leq x \leq 20$ cm , $y = 0$ cm). The

185 temperature of the solid ice at the top boundary ($y = 20$ cm) is maintained at 0 °C and the other surfaces (left and right sides)

are insulated (Fig. 3-a). Figure 3-b shows the temperature distribution after 5 hours modelled in the present work. Temperature profiles at *x*=4 cm and *x*=16 cm in different times of melting can be seen in Fig. 3-c and d, respectively. The result of our model is in good agreement with (Kahraman et al., 1998).
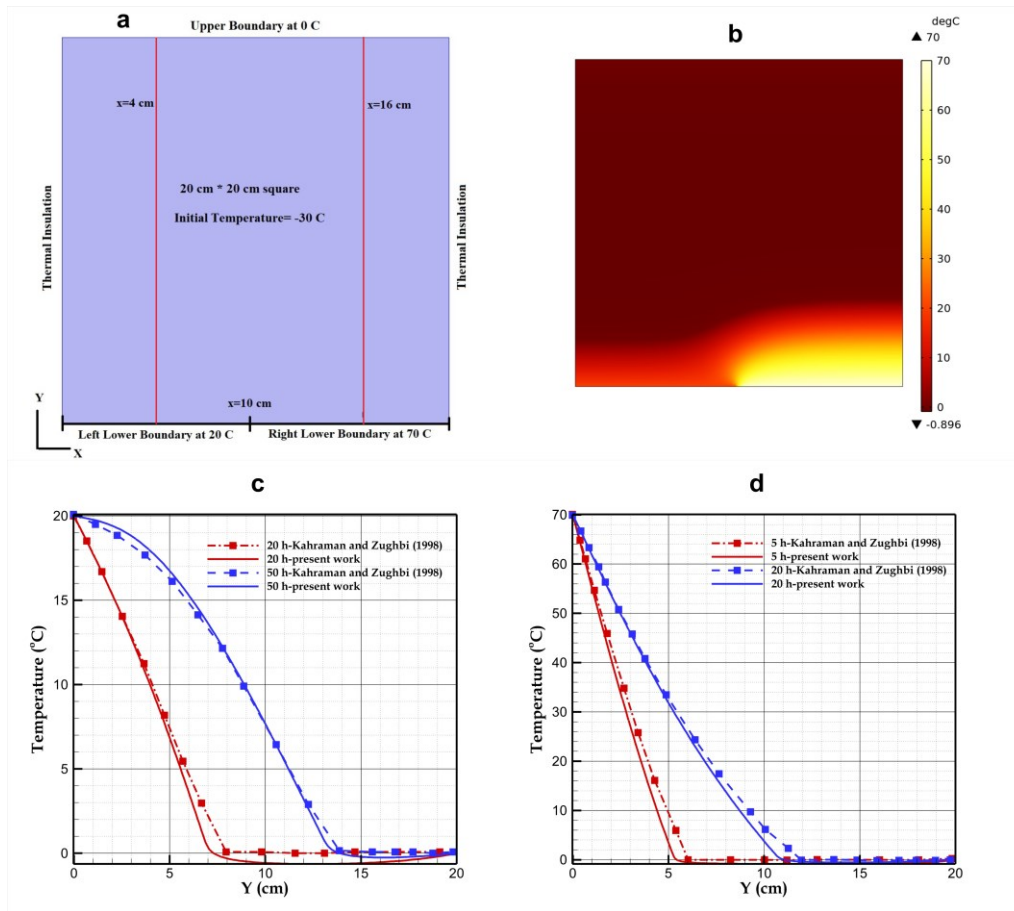
Figure 3. a) model geometry including initial and boundary conditions b) contour of temperature at t=5 hr c) temperature profile of ice and water at different times of ice melting at *x*=4 cm and d) *x*=16 cm

190

3.2 Free convection

Virag et al., (2006) investigated the effect of free convection on ice melting inside a cavity shown in Fig. 4-a. The lower and top surfaces are thermally insulated. The left and right boundaries are at 0 and 8 °C, respectively. Figure 4-b displays contours of temperature (left) and the velocity field as well as velocity vectors (right) predicted by our model. The black arrows indicate the direction of the water flow. The model predicts the existence of two contra-rotating free convection cells separated by the

4°C isotherm, which corresponds to the maximum liquid water density. In the small cell located in the lower left corner, where temperature is higher than 4°C, the liquid rises upward along the warm wall, as expected when the liquid density is a decreasing function of temperature. In the bigger cell located in the upper part of the liquid region, where the temperature is less than 4°C, the warmer liquid moves downward, as expected when the liquid density increases with temperature. Furthermore, results

200 show that where the temperature gradient is high, the magnitude of the local velocity increases. This is seen next to the left boundary and also close to the ice interface. The convection-induced mixing homogenizes the temperature in the liquid phase. Our numerical model replicates the melting front positions measured at different times by Virag et al. (2006) (see Fig. 5). Although some discrepancies exist between the experiments and the numerical model, especially at the bottom of the cavity at the beginning of the simulation and in the upper part at later times, the overall performance of our model is suitable to

205 represent the free convection cells and their effect on ice melting despite the simplifying assumptions made in the model (2D geometry, negligible volume contraction upon melting, smooth solid-liquid transition).
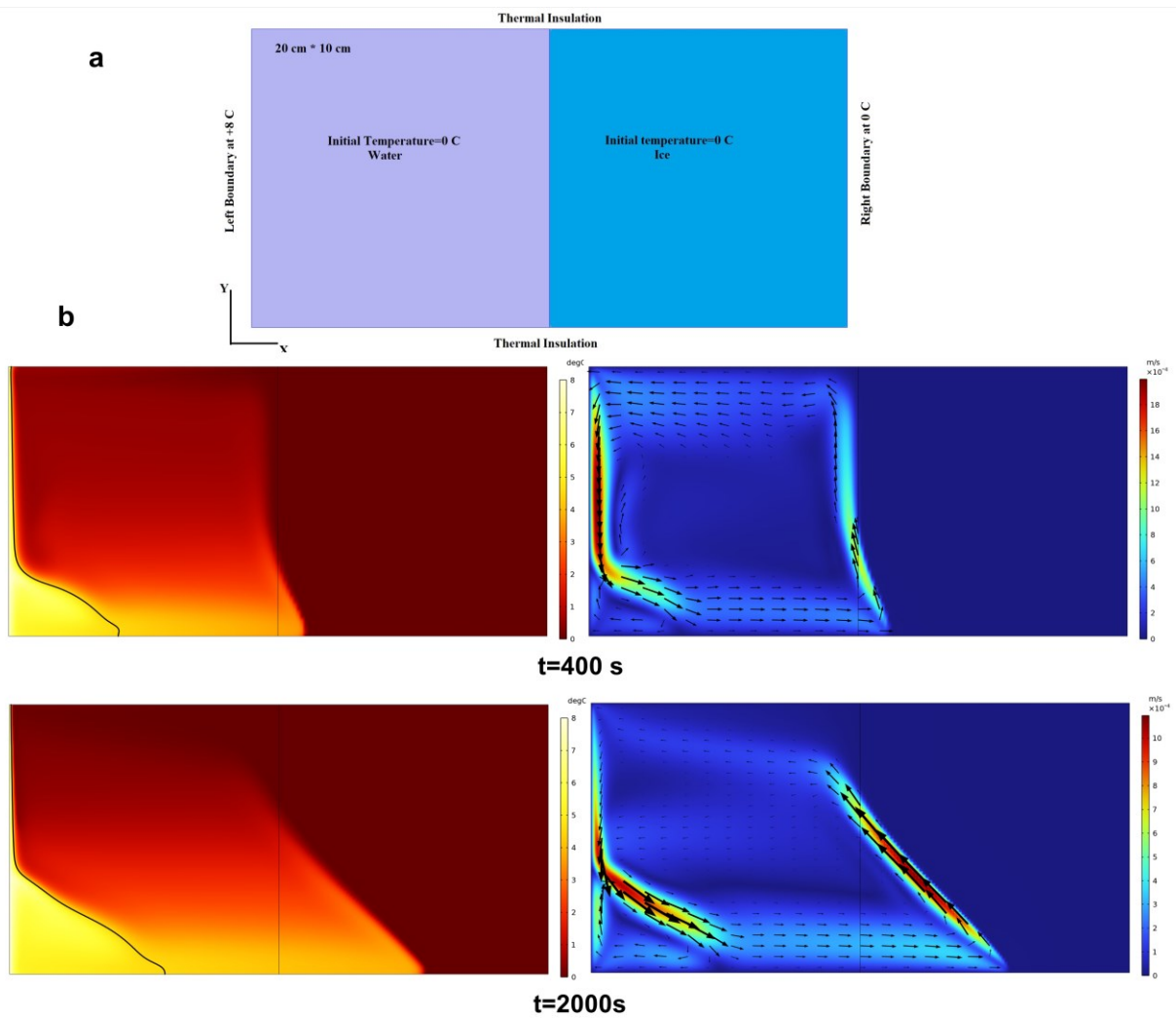
Figure 4. a) Computational domain including boundary and initial conditions in (Virag et al., 2006), b) results at times *t*=400 and 2000 s; left: temperature (the black line represents the isotherm *T*=4 °C); right: velocity magnitude.
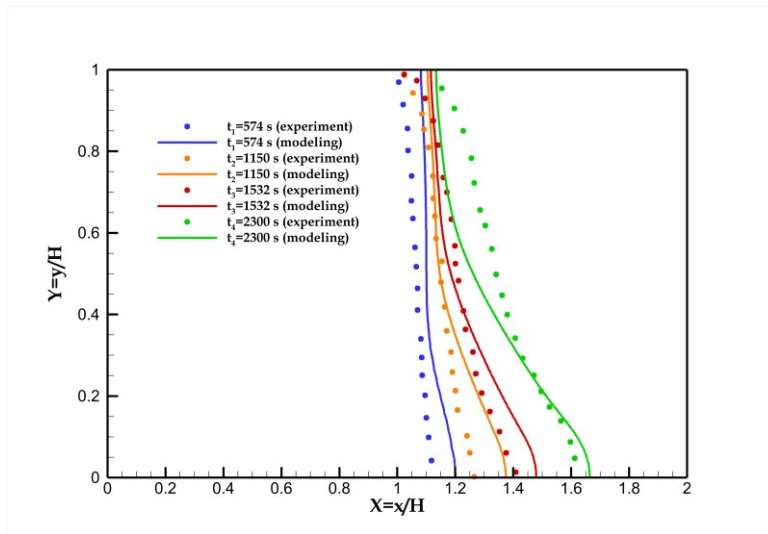
Figure 5. Evolution of the modeled ice-water interface during melting in comparison with experimental data by (Virag et al., 2006)

4 Results

4.1 Stagnant liquid water (SLW) versus free convection (FC)The effect of free convection in heterogeneous, ice-filled karst environment (cf Fig. 1), where the medium is surrounded by rock and prone to atmospheric warming from the top surface was conceptualized in section-2. Here, we investigate the effect of free convection in more details considering two scenarios under identical thermal settings: 1) stagnant liquid water (SLW) and 2) free convection in liquid water (FC). Figure 6 illustrates the ice volume fraction $(1 - \theta)$ for different time steps at 3, 6 and 9 hours for these two scenarios, for an aperture size A_p=10 cm (see Fig. 1-b for a description of the computational domain geometry). For each specified time step, the SLW results are shown on the left and the FC results on the right. The difference between these two scenarios in terms of melting rate is obvious. When disregarding convection (SLW), a uniform horizontal interface is observed between ice and water and an extreme slope is only observed next to the wall due to the greater thermal diffusivity of rock when compared to water. In fact, the conductive flux through the rock propagates faster than in water and melts the lateral side of the ice. In contrast, the presence of convection cells results in a curved interface between ice and liquid and the total volume of liquid water is noticeably higher compared to SLW.
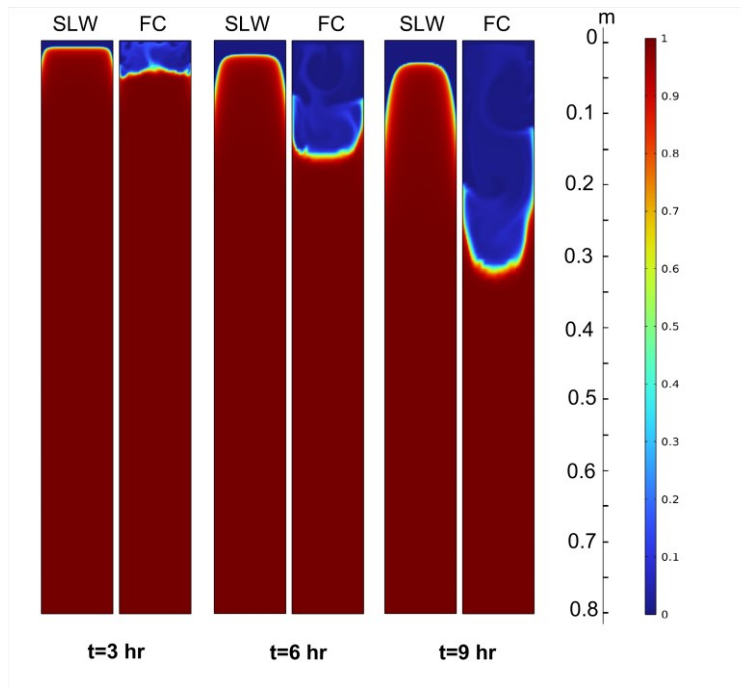
Figure 6. contour of the ice volume fraction $(1 - \theta)$ for stagnant liquid water (SLW) and free convection (FC). A_p=10 cm, H_{dom}=0.8 m and W=1 m .

220 Figure 7 displays the melting rate for both previous scenarios, SLW and FC. Because the initial temperature was -1 °C, the melting starts with c.1h delay, in both cases. Then the melting rate and the meltwater depth increase with time in response to the temperature increase at the top surface. After 9 hours, the melting rate is nearly an order of magnitude larger for FC (5.1 kg/s) than for SLW (0.6 kg/s). An animation file showing the evolution of the ice fraction can be found in the video supplement of the manuscript (Sedaghatkish and Luetscher, n.d.).

225 Figure 8 displays the temperature field of ice, water and surrounding rock after 9 hours. In FC case, most of the melted part of the cleft is in the temperature range from 0 to 1°C, with a high temperature gradient localized in a thin layer close to the ground surface (Fig. 8-b). In contrast, the temperature field in SLW case varies more evenly from the ground surface to the melting front (Fig. 8-a). This shows that the circulation of water inside the cleft results in a thermal bridge between ice interface and top atmosphere. The extent of the mixing zone induced by FC can be much higher than the diffusion length in the case of 230 SLW.

Figure-9 displays the left wall temperature as function of depth at different times for both scenarios. Although the melting rate for FC at t=3 hr is much higher than for SLW at the same time, their corresponding wall temperatures are close from each other. At larger times, the distinction between scenarios becomes more pronounced due to the increasing intensity of free convection.

235
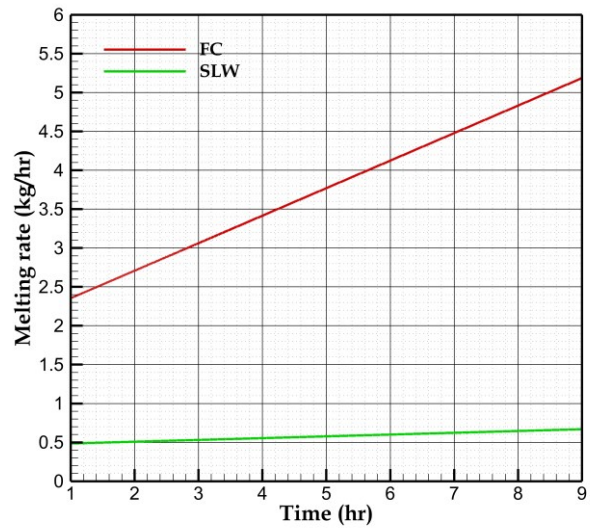
Figure 7. Melting rate versus time considering stagnant liquid water (SLW) and free convection (FC).
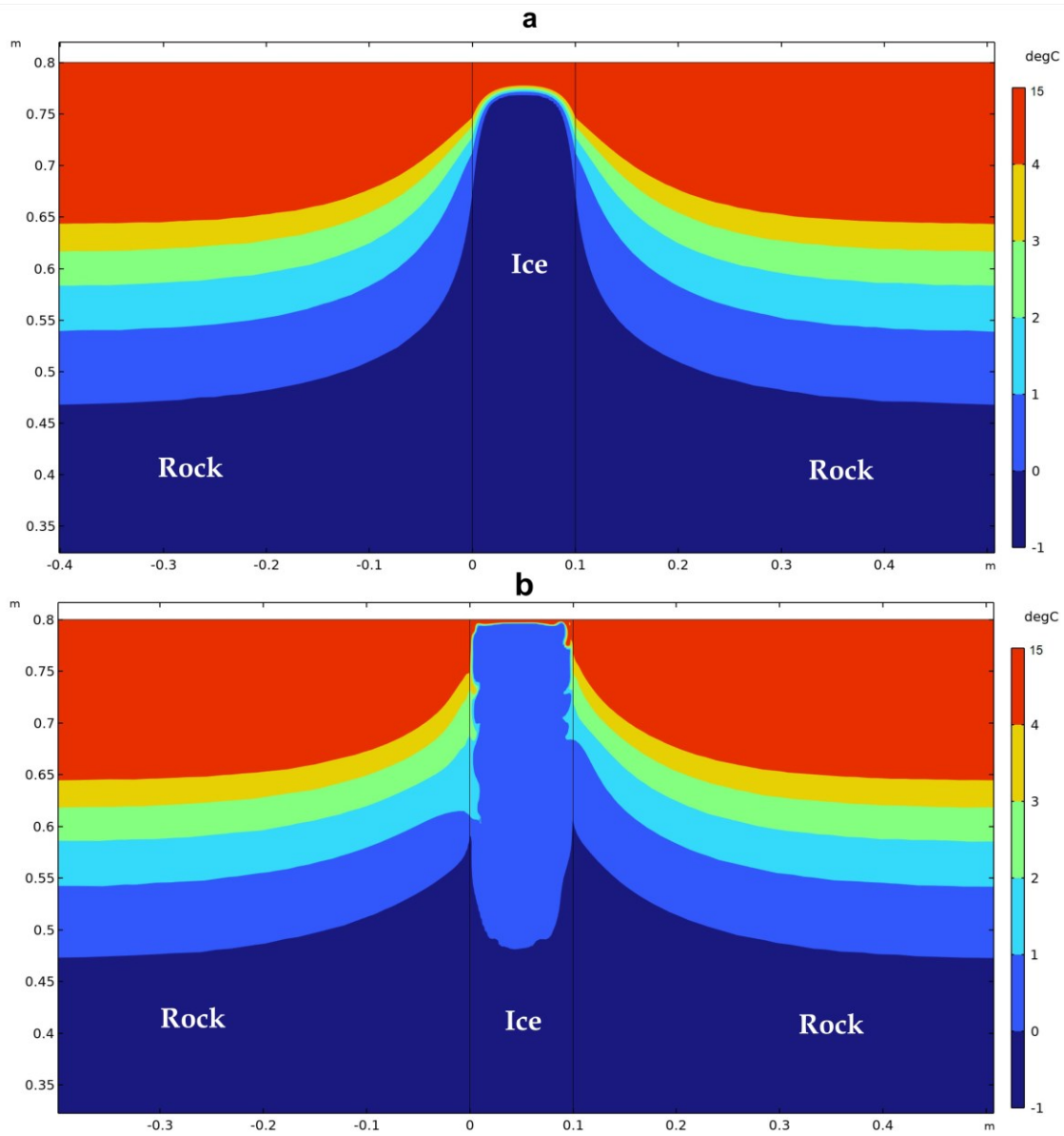
Figure 8. Temperature contour at t=9 hr for a) stagnant liquid water (SLW) and b) free convection (FC).
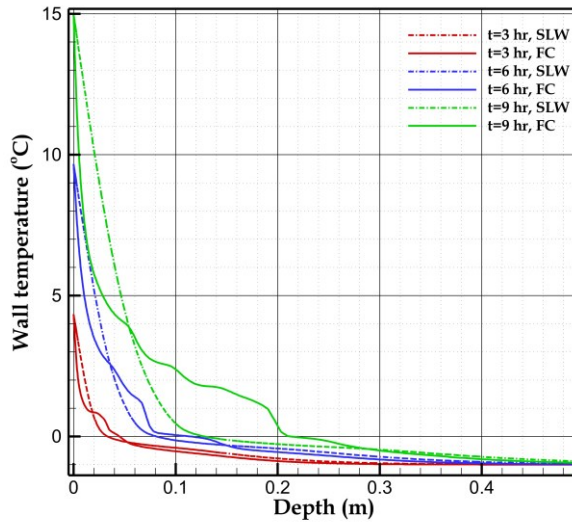
Figure 9. Left wall (rock-water interface) temperature as a function of depth) for stagnant liquid water (SLW) and free convection (FC).

Figure 10 displays the velocity magnitude as well as the flow in the water domain at different times. Vanishingly small velocity is predicted by the model wherever the water fraction is zero. Liquid water circulations generate a range of local velocities
240   mixing the water and homogenizing the water temperature. As the melting of ice advances and the meltwater amount increases the velocity of water within the mixing zone increases, thereby accentuating the significance of free convective flux.
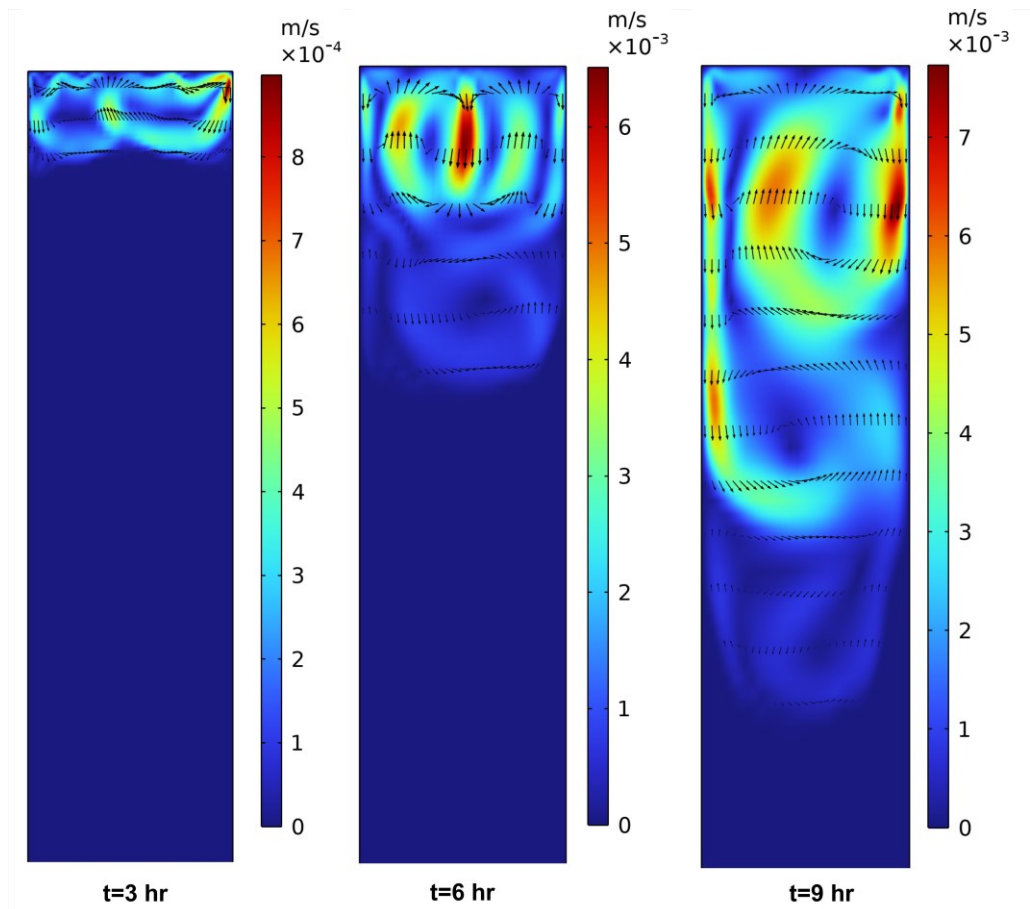
Figure 10. Velocity magnitude field in the upper 40 cm of the ice-cleft at different times. Zero velocity shows solid ice.

4.2 The effect of aperture size on melting rates

245 The cleft aperture determines the size of the domain and controls the initial ice mass. We considered the aperture sizes 2, 10, 20 and 50 cm in the parametric study. In order to remove the effect of cross-sectional area associated with different aperture sizes, we refer to the melting rate per unit of cross-sectional area (kg/hr/m^2).

Figure 11 illustrates the effect of the aperture size on the melting rate as a function of time. For the SLW case, increasing the aperture size to more than 10 cm does not have any effect on the melting rate. But, when the aperture size is smaller than a

250 certain value, the surrounding rock melts the ice more efficiently from the side walls due to its higher thermal diffusivity. In fact, the surrounding rock at a same depth has higher temperature than the ice filled cleft and when the aperture size is small enough this conductive heat flux propagates perpendicularly to the cleft and melts the ice. In the presence of free convection,

the melting rate after 9 hr is almost similar for the aperture sizes 2 and 10 cm (50 kg/hr/m²). For greater aperture sizes, the effect of free convection becomes more significant, resulting in the increase of the melting rate, which reaches about 110 kg/hr/m² for 50 cm aperture size. Figure 11 shows that the melting rate considering free convection with a 2 cm aperture-size (50 kg/hr/m²) is about twice the rate of the purely conduction case. For higher aperture sizes the difference in melting rates reaches about an order of magnitude.

In the present work, we simulated 9 hours of atmosphere temperature increase. When the aperture size A_p was varied from 2 to 50 cm, the liquid height H at the end of the simulation approximately ranged from 30 to 40 cm, and the convection cell occupied the entire liquid domain. However, the liquid height reached after 9 hours is only a small part of the actual height of the cleft (commonly up to 10 m). H is expected to increase if longer times are considered. The question arises whether the free convection cells always fill the entire liquid domain at longer times, despite the increase of friction due to lower aspect ratio A_p/H. If the convection cell occupies only a part of the cavity, the efficiency of heat transfer between the ground surface and the melting front will be reduced. The significance of free convection can be assessed from the value of the dimensionless Rayleigh number

$$Ra = \frac{g\beta(T_c - T_H)H^3}{\alpha_l \, \nu_l} \tag{15}$$

where $(T_c\text{-}T_H)$ is the temperature difference between bottom and top surfaces, $\alpha_l = k_l/(\rho_l c_{pl})$ and $\nu_l = \mu_l/\rho_l$ are the liquid water diffusivity and kinematic viscosity, respectively. Ra represents the ratio of the diffusion time over the free convection time ($Ra\sim10^8$ in the numerical experiments presented in this article). In a cavity with infinite lateral dimensions (i.e., for $A_p/H \to \infty$), free convection is triggered for $Ra \gtrsim 10^3$ (otherwise, the conductive state is stable, see Bergman et al., (2017) for more information about the Rayleigh-Bénard instability). However, in the confined geometry considered in this work, the presence of the vertical walls must be considered. Rohsenow et al (1998) provide the following condition for convection onset, which takes into account the stabilizing effect of the vertical walls for $A_p \ll H$, in the limiting case of perfectly conducting walls:

$$Ra \gtrsim 10^2 \times \left(\frac{H}{A_p}\right)^4 \tag{16}$$

Injecting Eq.(15) in Eq.(16) yields the maximum value of the liquid height H for which the free convection cell extends from the ground surface to the melting front:

$$H \lesssim 10^{-2} \times \frac{g\beta(T_c - T_H)A_p{}^4}{\alpha_l \, \nu_l} \tag{17}$$

Considering that the liquid region at temperature $T > 4°C$ is stable and that the isotherm 4°C is close to the top of the cleft when the free convection cell fills the entire cavity (see Fig. 8-b), we get $(T_c\text{-}T_H) = -4°C$. Using the physical properties from section

2.3 and $A_p = 2$ cm (the minimum aperture size considered in this study) yields $H \lesssim 10$ m, which is also the order of magnitude of the maximum cleft height. Therefore, free convection cells should always extend throughout the melted region for $A_p \gtrsim 2$ cm. Note that the assumption of perfectly conducting walls used in Eq.(16) is less favorable to convection than finite conductivity (Rohsenow et al, 1998). Eq.(17) is thus expected to underestimate the higher bound of H corresponding to fully developed free convection cells.
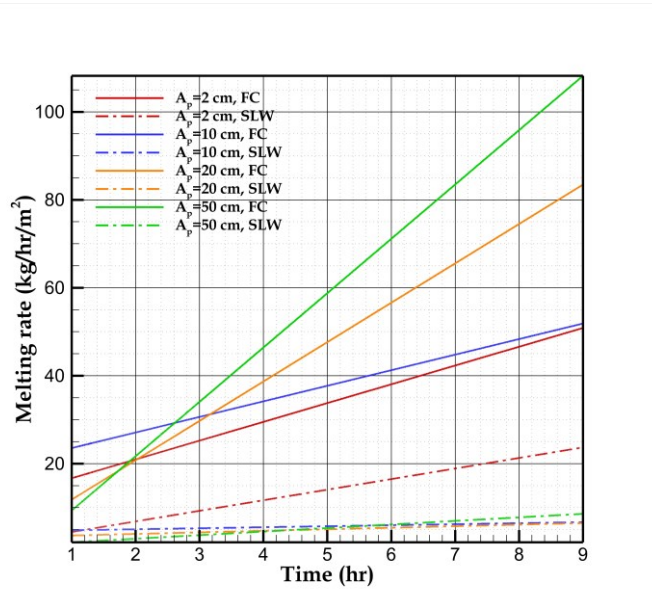
Figure 11. Effect of the aperture size on the melting rate for stagnant liquid water (SLW) and free convection (FC)

285

4.3 Application to field observations

The model is applied to a case-study from Monlesi ice cave, Switzerland (Luetscher et al., 2008). The main purpose is to qualitatively compare the field data with the model output and test how the pure conduction model can treat these problems. Monlesi ice cave is a low-elevation sporadic mountain permafrost site controlled by a peculiar ventilation regime associated with multiple cave entrances located at a similar elevation (Luetscher et al., 2008). The c. 600 m² cave chamber is partly filled with perennial congelation ice fed by a number of vertical clefts with width ranging from 10^1 to 10^3 mm. Seasonal freezing seals them periodically hindering any further water drainage from the epikarst (Fig. 12-a). The vertical distance between the external ground surface and the cave ceiling reaches c. 20 m. Seasonal and daily outside temperature fluctuations thaw the ice and freeze the meltwater in these rock clefts.

The main water inlet at Monlesi (subcutaneous flow) was instrumented to measure discharge rates at 30 min intervals using a pressure probe set at the bottom of a 1 m long perforated PVC tube capturing the inlet. The water height measured in the tube is converted to discharge (Q, in l/min) with an empirically calibrated rating curve checked by nine manual "bucket gauging" between 0 and 13 l/min with an uncertainty of ±10% (Luetscher et al., 2008).

Cave air temperatures were measured using negative temperature coefficient thermistors with a resistance of c.29.5 kOhm at 0°C and a temperature coefficient of about 5% °C-1 (YSI 44006). The thermistors were calibrated in a bath of melting ice to an accuracy of ±0.1°C. The thermistors were spaced at 2 m intervals in two chains comprising 19 sensors dispatched in the main cave chamber (Luetscher et al., 2008). Air temperatures were recorded at 1 h intervals and logged externally on a Campbell CR10X data logger with two multiplexer logging units.

Figure 12-b displays the atmosphere and the soil temperature at 10 cm depth during 4.5 days (from April 13 to 17). No rainfall is recorded during this time period and the surface is free of snow. The soil temperature increases with a regular trend between 0 and 5 °C and is noticeably attenuated compared to atmosphere temperature fluctuations. The cave temperature is almost constant around -1 °C implying there is no melting from the bottom of the ice cleft. The atmosphere daily temperature variation induces a water flow rate (0-12 l/min) with a trend similar to the surface temperature, supporting an origin associated with melting process of ice-filled clefts surrounding the cave.

To assess the melting rate, we considered the same conceptual model as in Fig. 1 with a linear temperature rise from 0 to 5 °C during 4.5 days at the top boundary (black dash-dotted in Fig. 12-b). In contrast to our model, meltwater drains deeper into the subsurface. The uncertainty about the cleft geometry is, however, very high and we do not know how many fissures feed this water inlet. While our conceptual model is based on a closed cavity for the ease of simulation, the ice-filled cleft can be connected to a network of partially saturated smaller clefts (as in the epikarst) which drain the meltwater to the main vertical inlet at the top wall of Monlesi cave. Eventually, our simplified 2D geometry only approaches the real 3D-environment since other convection cells emerge along the cavity width which cannot be modeled in 2D.

A rough estimate of the cavity geometry (computational domain) assumes an initial ice-filled cleft with 3 meters depth (H_{dom}=3 m),10 cm aperture size (A_p=10 cm) and a typical length in the order of 1 m. The cleft is subject to a linear temperature rise at the top boundary (black dash-dotted in Fig. 12-b). The modelled melting rate is in the same order of magnitude as the water flow rate measured in the cave (red dash-dotted in Fig. 12-b). A purely conduction-based model underestimates the melting rate by >1 order of magnitude as compared to the case considering free convection (dashed in Fig. 12-b).
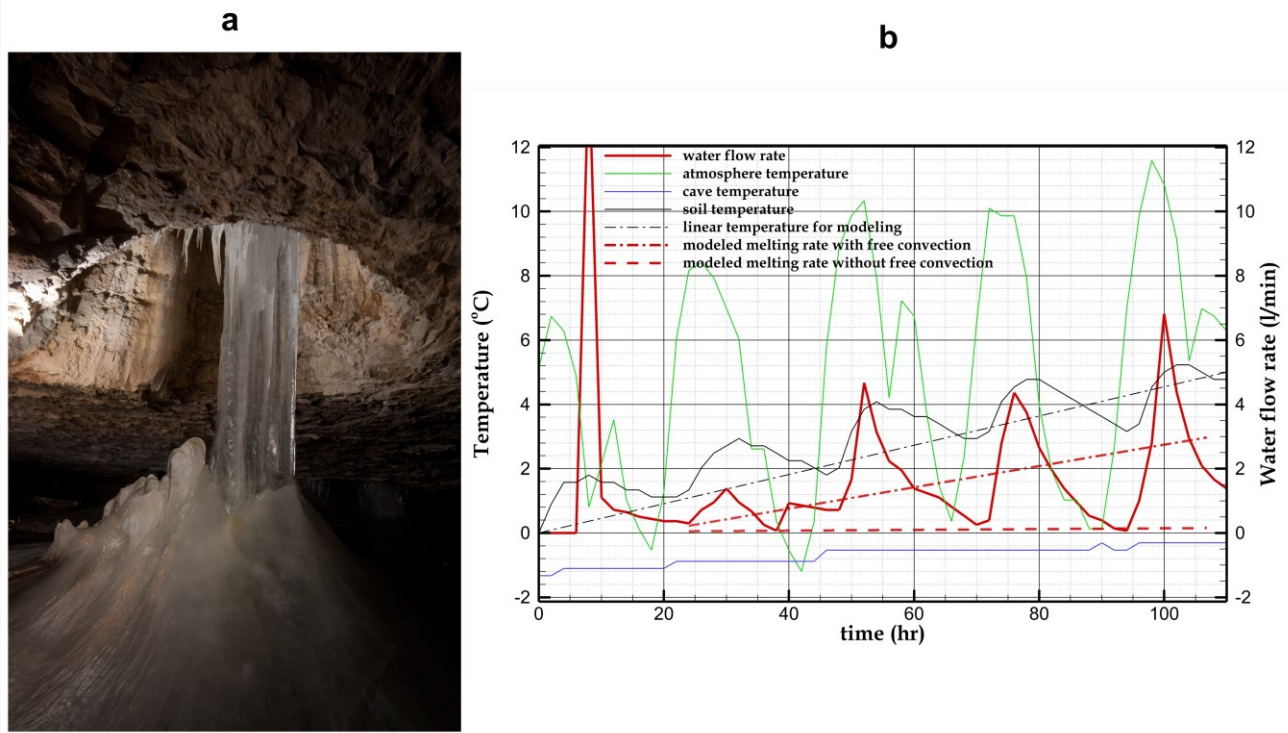
Figure 12. a) ice filled cleft in Monlesi cave b) field data including atmosphere (green), the soil (black) and cave temperature (blue) as well as the water flow rate measured at the fissure outlet (red) in Monlesi cave. The modelled melting rate considering free convection (red dashed dotted line) is compared to a case including only heat conduction (red dashed lines).

5 Discussion

A quantification of the melting rate of ice-rich permafrost in heterogeneous media is essential to assess the speed of permafrost degradation. Our model relies on a 2D approach coupling free convection (buoyancy-driven flow) in a vertical cleft with conduction in the surrounded homogeneous rock. Increasing the temperature of the ground surface can generate free convection cells because water-density increases between 0 and 4°C (a property specific to water). The convection cells generate a thermal bridge between the atmosphere and the melting front, resulting in the formation of a mixing zone with quasi-uniform temperature in the water column. This dramatically enhances the melting rate of interstitial ice when compared to ~~conventional,~~ purely conduction-based models assuming stagnant liquid water (about an order of magnitude after 9 hours for an aperture size of 10 cm). In contrast to scenarios assuming conduction in stagnant liquid water, for which the temperature signal from the atmosphere is fully attenuated beyond a certain distance known as the diffusion length, the presence of free convection extends over greater distances (Fig. 8-b). This thermal penetration also exerts an influence on the surrounding rock. Despite simplifying assumptions in the model and many uncertainties about the cleft geometry and the measured water flow rate, melting rate predicted by a model including free convection fit the order of magnitude measured in Monlesi cave (Fig. 12).

In this study, we assumed a constant aperture size for modeling ice melt at daily time scale, but it should be noted that in the long-term, the repeated freeze-thaw cycles can deteriorate the hostrock clefts due to propagation and coalescence of older ones.

340 Maji and Murton (Maji and Murton, 2021) investigated the mechanism and transition of microcracking and macrocracking during freezing and thawing and developed a statistical modeling of crack propagation dynamics based on tension and shearing. Our results show that, under similar thermal configurations, conduction may not be the principal heat flux and permafrost degradation in heterogenous and ice-rich media may be much faster than anticipated. This is particularly relevant at high-elevation where a clear relationship is observed between rockfall activity and permafrost thawing (Gruber et al., 2004; Ravanel

345 and Deline, 2011; Savi et al., 2021; Morino et al., 2021). In karst systems and fractured aquifers, where secondary porosity is exceptionally well developed, frozen conduits/fractures may all of a sudden drain water into depth and change the local hydrological regime leading a thermal anomaly within the surrounding permafrost (Phillips et al., 2016). The subsequent freeze-thaw processes may lead to the precipitation of so-called cryogenic cave calcites (Žák et al., 2018), a secondary mineral precipitate increasingly used as proxy for paleo-permafrost conditions (Spötl et al., 2021; Töchterle et al., 2023). In contrast

350 to purely conductive systems, our results support a model where rapid hydrological recharge, e.g. due to extreme rainfall events, may accelerate the thawing of mountain permafrost (Luetscher et al., 2013) and thus questions classical interpretations for the formation of cryogenic calcites. But also at shallower depth, acknowledging the potential role of convective heat fluxes in ice-rich permafrost degradation may help predicting the rate of greenhouse gas releases, mainly carbon dioxide and methane, due to the decomposition of formerly frozen organic matter (Schaefer et al., 2014; Schuur et al., 2015). The intensity of free

355 convection in soil depends strongly on the Rayleigh number which in turns depends on the permeability and dimensions of soil layer making it negligible, e.g. (Kane et al., 2001) or significant, e.g. (Jazi et al., 2024) with respect to the total heat transfer.

Pure water with a melting point at 0°C was considered in the present study. However, limestone dissolution results in the mineralization of the meltwater. Consequences are twofold: (1) the melting point is shifted to lower temperatures (in the range

360 from -4 °C to 0 °C, see Tubini et al. (2021); McKenzie et al. (2007); Rühaak et al. (2015); (2) the variation of density with salt concentration could impact buoyancy, resulting in different flow patterns (thermosolutal convection, see for instance Mergui et al., (2002) resulting in different flow patterns. The significance of the liquid phase composition could be assessed by numerical simulations, and should be considered in future works.

We did not consider any drainage of air or water inside the cleft or in its immediate vicinity. Forced convection induced by

365 drainage could also contribute to the formation of a thermal bridge between the ground surface and the melting front, as suggested by Hasler et al., (2011). More work coupling field observations with numerical simulations including forced and free convection will be necessary to assess their relative significance, and determine the conditions under which one or the other effect dominates heat transfer.

6 Conclusion

370 In heterogeneous and ice-rich media, a model considering only conduction underestimate melting rates of frozen rock clefts. Free convection gives rise to a mixing zone characterized by a uniform temperature. This zone has the potential to extend beyond the length typically associated with diffusion. Free convection can increase the melting rate by one order of magnitude. Importantly, the presence of this mixing zone does not only impact the temperature distribution within the water, but also affects the surrounding rock.

375 The effect of free convection vanishes with decreasing aperture size, typically < 2 cm at 8 m meltwater depth, when the viscous force at the wall dominates buoyancy forces. In this case, ice melting is driven by conduction.

The significance of free convection should also be estimated in similar thermal configurations with different geometries such as cylindrical conduits or 3D cavities. Furthermore, the effect of free convection is not limited to hourly or daily oscillations and can be studied over much longer timescales, including centennial to millennial fluctuations. Currently, the computational

380 costs are the main barriers for including free convection in long-term simulations. The full coupling of the momentum and energy equations requires the time steps being much smaller compared to simple conduction-based models. Further investigations are thus ongoing to reformulate the governing equations and simplifying them for simulations over longer time-scales. Moreover, refreezing processes have yet to be considered to fully represent the long-term evolution of such a system. Eventually, the effect of water free convection on ice melting rate is not limited to permafrost regions. For instance, the melting

385 of icebergs can also be impacted by water free convection (Couston et al., 2021; Hester et al., 2021) increasing production of freshwater in oceans with potential impacts on the climate at global scale.

390 **Appendix A: Sensitivity of the model to the melting temperature range ΔT.**

The sensitivity of the melting rate to the melting temperature range ΔT is displayed in Fig.A1. Similar results are obtained for $\Delta T \leq \pm 0.7°C$. $\Delta T \leq \pm 0.5°C$ was thus selected in all simulations, as a value giving a good approximation of the pure water melting rate.
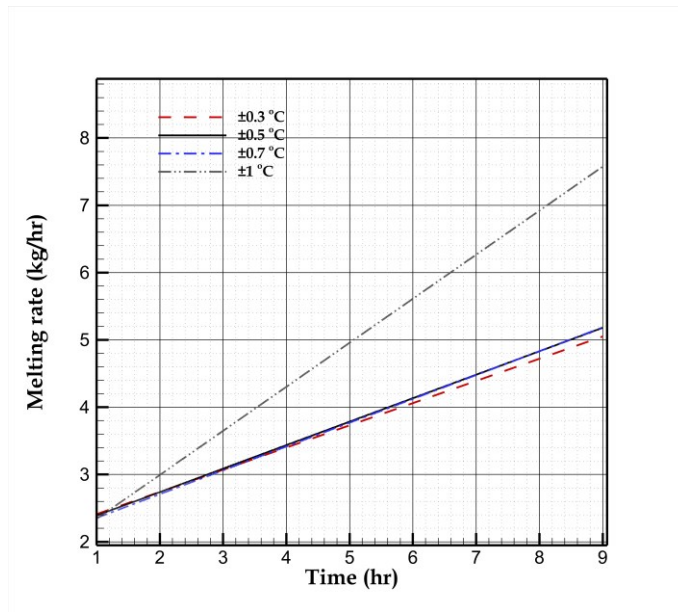
Figure A1. Effect on the melting temperature range ΔT on the melting rate predicted by the model (FC case, A_p=10 cm, H_{dom}=0.8 m, W_{dom}= 1 m .)

395

Software availability. The Comsol file (closed source software) is available upon request.

400

Video supplement. The animations of ice fraction evolution are available at https://doi.org/10.5281/zenodo.8435168.

Author contributions. AS completed the modelling work and wrote the original manuscript. ML designed the study together with AS and contributed with field data from Monlesi ice cave. All authors discussed the results and contributed to the final
405 edition of the paper.

Competing interests. The authors declare that they have no competing interests.

410 *Acknowledgements.* This project is supported by the Swiss National Science Foundation (project n°200021_188636).

Reference

Andresen, C. G., Lawrence, D. M., Wilson, C. J., McGuire, A. D., Koven, C., Schaefer, K., Jafarov, E., Peng, S., Chen, X., and Gouttevin, I.: Soil moisture and hydrology projections of the permafrost region– a model intercomparison, Cryosph., 14, 445–459, 2020.

Bartelt, P. and Lehning, M.: A physical SNOWPACK model for the Swiss avalanche warning: Part I: numerical model, Cold Reg. Sci. Technol., 35, 123–145, 2002.

Bartolomé, M., Cazenave, G., Luetscher, M., Spötl, C., Gázquez, F., Belmonte, Á., Turchyn, A. V., López-Moreno, J. I., and Moreno, A.: Mountain permafrost in the Central Pyrenees: insights from the Devaux ice cave, Cryosph., 17, 477–497, 2022.

Bejan, A.: Convection heat transfer, John wiley & sons, 2013.

Bense, V. F., Kooi, H., Ferguson, G., and Read, T.: Permafrost degradation as a control on hydrogeological regime shifts in a warming climate, J. Geophys. Res. Earth Surf., 117, 2012.

Bergman, T. L., Lavine, A. S., Incropera, F. P., and DeWitt, D. P.: Fundamentals of Heat and Mass Transfer, Wiley, 2017.

Caggiano, A., Mankel, C., and Koenders, E.: Reviewing theoretical and numerical models for PCM-embedded cementitious composites, Buildings, 9, 3, 2018.

Cheng, G.: A roadbed cooling approach for the construction of Qinghai–Tibet Railway, Cold Reg. Sci. Technol., 42, 169–176, 2005.

Cicoira, A., Beutel, J., Faillettaz, J., Gärtner-Roer, I., and Vieli, A.: Resolving the influence of temperature forcing through heat conduction on rock glacier dynamics: a numerical modelling approach, Cryosph., 13, 927–942, 2019.

Colucci, R. R. and Guglielmin, M.: Climate change and rapid ice melt: Suggestions from abrupt permafrost degradation and ice melting in an alpine ice cave, Prog. Phys. Geogr. Earth Environ., 43, 561–573, 2019.

Comsol, A. B.: Heat Transfer Module User Guide, 2018.

Couston, L.-A., Hester, E., Favier, B., Taylor, J. R., Holland, P. R., and Jenkins, A.: Topography generation by melting and freezing in a turbulent shear flow, J. Fluid Mech., 911, A44, 2021.

Covington, M. D., Luhmann, A. J., Gabrovšek, F., Saar, M. O., and Wicks, C. M.: Mechanisms of heat exchange between water and rock in karst conduits, Water Resour. Res., 47, 2011.

Duvillard, P.-A., Ravanel, L., Schoeneich, P., Deline, P., Marcer, M., and Magnin, F.: Qualitative risk assessment and strategies for infrastructure on permafrost in the French Alps, Cold Reg. Sci. Technol., 189, 103311, 2021.

Fabre, C., Sauvage, S., Tananaev, N., Srinivasan, R., Teisserenc, R., and Sánchez Pérez, J. M.: Using modeling tools to better understand permafrost hydrology, Water, 9, 418, 2017.

Fohlmeister, J., Luetscher, M., Spötl, C., Schröder-Ritzrau, A., Schröder, B., Frank, N., Eichstädter, R., Trüssel, M., Skiba, V., and Boers, N.: The role of Northern Hemisphere summer insolation for millennial-scale climate variability during the

penultimate glacial, Commun. Earth Environ., 4, 245, 2023.

445 Ford, D. and Williams, P. D.: Karst hydrogeology and geomorphology, John Wiley & Sons, 2007.

Fortier, R., LeBlanc, A.-M., and Yu, W.: Impacts of permafrost degradation on a road embankment at Umiujaq in Nunavik (Quebec), Canada, Can. Geotech. J., 48, 720–740, 2011.

Galushkin, Y.: Numerical simulation of permafrost evolution as a part of sedimentary basin modeling: permafrost in the Pliocene–Holocene climate history of the Urengoy field in the West Siberian basin, Can. J. Earth Sci., 34, 935–948, 1997.

450 Gruber, S., Hoelzle, M., and Haeberli, W.: Permafrost thaw and destabilization of Alpine rock walls in the hot summer of 2003, Geophys. Res. Lett., 31, 2004.

Guerrier, B., Doumenc, F., Roux, A., Mergui, S., and Jeannin, P.-Y.: Climatology in shallow caves with negligible ventilation: Heat and mass transfer, Int. J. Therm. Sci., 146, 106066, 2019.

Guyon, E., Hulin, J. P., Petit, L., and Mitescu, C. D.: Physical hydrodynamics, Oxford university press, 2015.

455 Haberkorn, A., Kenner, R., Noetzli, J., and Phillips, M.: Changes in ground temperature and dynamics in mountain permafrost in the Swiss Alps, Front. Earth Sci., 9, 626686, 2021.

Haeberli, W., Schaub, Y., and Huggel, C.: Increasing risks related to landslides from degrading permafrost into new lakes in de-glaciating mountain ranges, Geomorphology, 293, 405–417, 2017.

Hasler, A., Gruber, S., Font, M., and Dubois, A.: Advective heat transport in frozen rock clefts: Conceptual model, laboratory 460 experiments and numerical simulation, Permafr. Periglac. Process., 22, 378–389, 2011.

Hayward, J. L., Jackson, A. J., Yost, C. K., Hansen, L. T., and Jamieson, R. C.: Fate of antibiotic resistance genes in two Arctic tundra wetlands impacted by municipal wastewater, Sci. Total Environ., 642, 1415–1428, 2018.

Heitz, W. L. and Westwater, J. W.: Extension of the numerical method for melting and freezing problems, Int. J. Heat Mass Transf., 13, 1371–1375, 1970.

465 Hester, E. W., McConnochie, C. D., Cenedese, C., Couston, L.-A., and Vasil, G.: Aspect ratio affects iceberg melting, Phys. Rev. Fluids, 6, 23802, 2021.

Hornum, M. T., Hodson, A. J., Jessen, S., Bense, V., and Senger, K.: Numerical modelling of permafrost spring discharge and open-system pingo formation induced by basal permafrost aggradation, Cryosph., 14, 4627–4651, 2020.

Huss, M., Farinotti, D., Bauder, A., and Funk, M.: Modelling runoff from highly glacierized alpine drainage basins in a 470 changing climate, Hydrol. Process., 22, 3888–3902, 2008.

Ivanov, V. and Rozhin, I.: Numerical simulation of the permafrost thawing near the city of Yakutsk during climate change up to the year 2100, in: AIP Conference Proceedings, 20050, 2022.

Jafarov, E. E., Marchenko, S. S., and Romanovsky, V. E.: Numerical modeling of permafrost dynamics in Alaska using a high spatial resolution dataset, Cryosph., 6, 613–624, 2012.

475 Jazi, F. N., Ghasemi-Fare, O., and Rockaway, T. D.: Natural convection effect on heat transfer in saturated soils under the influence of confined and unconfined subsurface flow, Appl. Therm. Eng., 237, 121805, 2024.

Jin, X.-Y., Jin, H.-J., Iwahana, G., Marchenko, S. S., Luo, D.-L., Li, X.-Y., and Liang, S.-H.: Impacts of climate-induced

permafrost degradation on vegetation: A review, Adv. Clim. Chang. Res., 12, 29–47, 2021.

Kahraman, R., Zughbi, H. D., and Al-Nassar, Y. N.: A numerical simulation of melting of ice heated from above, Math.

480   Comput. Appl., 3, 127–137, 1998.

Kane, D. L., Hinkel, K. M., Goering, D. J., Hinzman, L. D., and Outcalt, S. I.: Non-conductive heat transfer associated with frozen soils, Glob. Planet. Change, 29, 275–292, 2001.

Krumhansl, K. A., Krkosek, W. H., Greenwood, M., Ragush, C., Schmidt, J., Grant, J., Barrell, J., Lu, L., Lam, B., and Gagnon, G. A.: Assessment of Arctic community wastewater impacts on marine benthic invertebrates., Environ. Sci. Technol., 49, 760–

485   766, 2015.

Larsen, P. H., Goldsmith, S., Smith, O., Wilson, M. L., Strzepek, K., Chinowsky, P., and Saylor, B.: Estimating future costs for Alaska public infrastructure at risk from climate change, Glob. Environ. Chang., 18, 442–457, 2008.

Luetscher, M., Lismonde, B., and Jeannin, P.: Heat exchanges in the heterothermic zone of a karst system: Monlesi cave, Swiss Jura Mountains, J. Geophys. Res. Earth Surf., 113, 2008.

490   Luetscher, M., Borreguero, M., Moseley, G. E., Spötl, C., and Edwards, R. L.: Alpine permafrost thawing during the Medieval Warm Period identified from cryogenic cave carbonates, Cryosph., 7, 1073–1081, 2013.

Luetscher, M., Boch, R., Sodemann, H., Spötl, C., Cheng, H., Edwards, R. L., Frisia, S., Hof, F., and Müller, W.: North Atlantic storm track changes during the Last Glacial Maximum recorded by Alpine speleothems, Nat. Commun., 6, 6344, 2015.

Maji, V. and Murton, J. B.: Experimental observations and statistical modeling of crack propagation dynamics in limestone by

495   acoustic emission analysis during freezing and thawing, J. Geophys. Res. Earth Surf., 126, e2021JF006127, 2021.

Malakhova, V. V: Numerical modeling of methane hydrates dissociation in the submarine permafrost, in: IOP Conference Series: Earth and Environmental Science, 12022, 2022.

Marchenko, S., Romanovsky, V., and Tipenko, G.: Numerical modeling of spatial permafrost dynamics in Alaska, in: Proceedings of the ninth international conference on permafrost, 1125–1130, 2008.

500   McKenzie, J. M., Voss, C. I., and Siegel, D. I.: Groundwater flow with energy transport and water–ice phase change: numerical simulations, benchmarks, and application to freezing in peat bogs, Adv. Water Resour., 30, 966–983, 2007.

Mergui, S., Geoffroy, S., and Be´nard, C.: Ice block melting into a binary solution: Coupling of the interfacial equilibrium and the flow structures, J. Heat Transf., 124, 1147–1157, 2002.

Mohammed, A. A., Bense, V. F., Kurylyk, B. L., Jamieson, R. C., Johnston, L. H., and Jackson, A. J.: Modeling reactive solute

505   transport in permafrost-affected groundwater systems, Water Resour. Res., 57, e2020WR028771, 2021.

Morino, C., Conway, S. J., Balme, M. R., Helgason, J. K., Sæmundsson, Þ., Jordan, C., Hillier, J., and Argles, T.: The impact of ground-ice thaw on landslide geomorphology and dynamics: two case studies in northern Iceland, Landslides, 18, 2785–2812, 2021.

Mousavi Ajarostaghi, S. S., Poncet, S., Sedighi, K., and Aghajani Delavar, M.: Numerical modeling of the melting process in

510   a shell and coil tube ice storage system for air-conditioning application, Appl. Sci., 9, 2726, 2019.

Nazzi Ehms, J. H., De Césaro Oliveski, R., Oliveira Rocha, L. A., Biserni, C., and Garai, M.: Fixed grid numerical models for

solidification and melting of phase change materials (PCMs), Appl. Sci., 9, 4334, 2019.

Noetzli, J., Arenson, L. U., Bast, A., Beutel, J., Delaloye, R., Farinotti, D., Gruber, S., Gubler, H., Haeberli, W., and Hasler, A.: Best practice for measuring permafrost temperature in boreholes based on the experience in the Swiss Alps, Front. Earth

515 Sci., 9, 607875, 2021.

Painter, S. L., Coon, E. T., Atchley, A. L., Berndt, M., Garimella, R., Moulton, J. D., Svyatskiy, D., and Wilson, C. J.: Integrated surface/subsurface permafrost thermal hydrology: Model formulation and proof-of-concept simulations, Water Resour. Res., 52, 6062–6077, 2016.

Pelletier, M., Allard, M., and Levesque, E.: Ecosystem changes across a gradient of permafrost degradation in subarctic Québec

520 (Tasiapik Valley, Nunavik, Canada), Arct. Sci., 5, 1–26, 2018.

Pham, H.-N., Arenson, L. U., and Sego, D. C.: Numerical analysis of forced and natural convection in waste-rock piles in permafrost environments, in: Proceedings of the Ninth International Conference on Permafrost, 2008.

Phillips, M., Haberkorn, A., Draebing, D., Krautblatter, M., Rhyner, H., and Kenner, R.: Seasonally intermittent water flow through deep fractures in an Alpine Rock Ridge: Gemsstock, Central Swiss Alps, Cold Reg. Sci. Technol., 125, 117–127,

525 2016.

Pruessner, L., Huss, M., Phillips, M., and Farinotti, D.: A framework for modeling rock glaciers and permafrost at the basin-scale in high alpine catchments, J. Adv. Model. Earth Syst., 13, e2020MS002361, 2021.

Ravanel, L. and Deline, P.: Climate influence on rockfalls in high-Alpine steep rockwalls: The north side of the Aiguilles de Chamonix (Mont Blanc massif) since the end of the 'Little Ice Age,' The Holocene, 21, 357–365, 2011.

530 Rohsenow, W. M., Hartnett, J. P., and Cho, Y. I.: Handbook of heat transfer, Mcgraw-hill New York, 1998.

Rühaak, W., Anbergen, H., Grenier, C., McKenzie, J., Kurylyk, B. L., Molson, J., Roux, N., and Sass, I.: Benchmarking numerical freeze/thaw models, Energy Procedia, 76, 301–310, 2015.

Savi, S., Comiti, F., and Strecker, M. R.: Pronounced increase in slope instability linked to global warming: A case study from the eastern European Alps, Earth Surf. Process. Landforms, 46, 1328–1347, 2021.

535 Schaefer, K., Lantuit, H., Romanovsky, V. E., Schuur, E. A. G., and Witt, R.: The impact of the permafrost carbon feedback on global climate, Environ. Res. Lett., 9, 85003, 2014.

Schuster, P. F., Schaefer, K. M., Aiken, G. R., Antweiler, R. C., Dewild, J. F., Gryziec, J. D., Gusmeroli, A., Hugelius, G., Jafarov, E., and Krabbenhoft, D. P.: Permafrost stores a globally significant amount of mercury, Geophys. Res. Lett., 45, 1463– 1471, 2018.

540 Schuur, E. A. G., McGuire, A. D., Schädel, C., Grosse, G., Harden, J. W., Hayes, D. J., Hugelius, G., Koven, C. D., Kuhry, P., and Lawrence, D. M.: Climate change and the permafrost carbon feedback, Nature, 520, 171–179, 2015.

Sedaghatkish, A. and Luetscher, M.: Modeling the effect of free convection on permafrost melting-rates in frozen rock-clefts, , https://doi.org/10.5281/zenodo.8435168, n.d.

Spötl, C., Koltai, G., Jarosch, A. H., and Cheng, H.: Increased autumn and winter precipitation during the Last Glacial

545 Maximum in the European Alps, Nat. Commun., 12, 1839, 2021.

Töchterle, P., Baldo, A., Murton, J. B., Schenk, F., Edwards, R. L., Koltai, G., and Moseley, G. E.: Reconstructing Younger Dryas Ground Temperature and Snow Thickness from Cave Deposits, Clim. Past Discuss., 2023, 1–21, 2023.

Tubini, N., Gruber, S., and Rigon, R.: A method for solving heat transfer with phase change in ice or soil that allows for large time steps while guaranteeing energy conservation, Cryosph., 15, 2541–2568, 2021.

550   Virag, Z., Živić, M., and Galović, A.: Influence of natural convection on the melting of ice block surrounded by water on all sides, Int. J. Heat Mass Transf., 49, 4106–4115, 2006.

Walvoord, M. A. and Kurylyk, B. L.: Hydrologic impacts of thawing permafrost—A review, Vadose Zo. J., 15, 2016.

Weast, R. C.: CRC handbook of chemistry and physics., 1986.

Wind, M., Obleitner, F., Racine, T., and Spötl, C.: Multi-annual temperature evolution and implications for cave ice

555   development in a sag-type ice cave in the Austrian Alps, Cryosph., 16, 3163–3179, 2022.

Žák, K., Onac, B. P., Kadebskaya, O. I., Filippi, M., Dublyansky, Y., and Luetscher, M.: Cryogenic mineral formation in caves, in: Ice caves, Elsevier, 123–162, 2018.

Zhang, M., Lai, Y., Liu, Z., and Gao, Z.: Nonlinear analysis for the cooling effect of Qinghai-Tibetan railway embankment with different structures in permafrost regions, Cold Reg. Sci. Technol., 42, 237–249, 2005.

560